

Supporting Information

Plasmon-Enhanced Light Absorption at Organic-Coated Interfaces: Collectivity Matters

**Note: on 8th February 2022 this file replaced the original version from
January 2018**

Alexandra I. Zvyagina,^a Alexander A. Ezhov,^{b,c} Ivan N. Meshkov,^a Vladimir K. Ivanov,^{d,e} Kirill P. Birin,^a Burkhard König,^f Yulia G. Gorbunova,^{a,d} Aslan Yu. Tsivadze,^{a,d} Vladimir V. Arslanov,^a and Maria A. Kalinina^{a,g*}

- a. A. N. Frumkin Institute of Physical Chemistry and Electrochemistry, Russian Academy of Sciences, 31 b 4 Leninsky prospect, Moscow 119071, Russia.
- b. Faculty of Physics, M. V. Lomonosov Moscow State University, Leninskiye Gory, GSP-1, Moscow 119991, Russia.
- c. A. V. Topchiev Institute of Petrochemical Synthesis, Russian Academy of Sciences, 29 Leninsky prospect, Moscow 119991, Russia.
- d. N. S. Kurnakov Institute of General and Inorganic Chemistry, Russian Academy of Sciences, 31 Leninsky prospect, Moscow 119991, Russia.
- e. Faculty of Materials Science, M.V. Lomonosov Moscow State University, 1-73 Leninskiye Gory, GSP-1, Moscow 119991, Russia.
- f. Institut für Organische Chemie, Universität Regensburg, D-93040 Regensburg, Germany.
- g. Department of Colloid Chemistry, Institute of Fine Chemical Technologies, Moscow Technological University, 86 Vernadsky Ave., Moscow 119571, Russia.

Content

Experimental Section

- S1. Optical efficiency as a parameter for comparison of optical properties of AuNPs and molecules of dyes
- S2. Properties of RuL(EIN)₂ chromophore in solution and Langmuir monolayers
- S3. Properties of TAMRA chromophore in solution and Langmuir monolayers
- S4. Properties of CeL₂ chromophore in solution and Langmuir monolayers
- S5. Properties of EP-PDI chromophore in solution and Langmuir monolayers
- S6. Properties of TPyP chromophore in solution and Langmuir-Blodgett films
- S7. Influence of the dielectric properties of surrounding media to the optical properties of AuNP
- S8. Numerical simulation of the near field of the AuNPs on the surface of support covered by dye layer
- S9. References

Experimental Section

Materials

All chemicals used were of analytical reagent grade. Cerium bis[tetra-(15-crown-5)-phthalocyaninate] (CeL_2) and ruthenium tetra-(15-crown-5)-phthalocyaninate with axially coordinated ethylisonicotinate molecules ($\text{RuL}(\text{EIN})_2$) were synthesized according to the procedures previously described in ⁶¹ and in ^{62,63}, respectively. 5-carboxytetramethylrhodamine (**TAMRA**), N,N'-bis(3-pentyl)perylene-3, 4, 9, 10-bis(dicarboximide) (**EP-PDI**), 5,10,15,20-tetra(4-pyridyl)-21H,23H-porphine (**TPyP**) was obtained from Sigma Aldrich. Potassium hydroxide was obtained from Labtekh (Russia). Chloroform (Merck) was used as a solvent for the preparation of $5 \cdot 10^{-5}$ M $\text{RuL}(\text{EIN})_2$, $1 \cdot 10^{-4}$ M TAMRA, $1 \cdot 10^{-5}$ M CeL_2 , $1.4 \cdot 10^{-4}$ M EP-PDI, $1.1 \cdot 10^{-4}$ M TPyP, $1 \cdot 10^{-3}$ M stearic acid (SA) and $1 \cdot 10^{-3}$ M octadecylamine (ODA) solutions. Gold hydrosol was synthesized by a common procedure for citrate reduction of HAuCl_4 ⁶⁴ (Acros Organics, Belgium) in water deionized to 16 M Ω cm resistivity. For as-prepared nanoparticles, the surface plasmon band appears at 519–520 nm in the UV–vis adsorption spectra. Average diameter of 18 ± 1 nm was routinely estimated from DLS data; the synthetic yield corresponds to a number of nanoparticles of $\sim 10^{15}$ L⁻¹. The pH of gold hydrosol was 6.7 ± 0.1 . The synthesis of cerium oxide hydrosol was reported elsewhere.⁶⁵ The pH of CeO_2 NPs hydrosol was 6.5 ± 0.1 ; DLS and TEM investigation gave an CeO_2 NPs average size of 3 nm with a comparatively wide size distribution.⁴⁸ To prepare mixed hydrosols with varied ratios of components, certain portions of gold and cerium oxide colloidal solutions were mixed directly and then appropriately diluted using 0.05 wt % sodium citrate solution.

Methods

Ultrathin Films Fabrication

KSV Minitrough (KSV Instrument Ltd., Helsinki, Finland) equipped with a Wilhelmy plate was used for ultrathin film fabrication. A Teflon trough with a surface area of 283 cm² was sequentially rinsed with acetone, chloroform and pure water. Polyacetal barriers were rinsed with ethanol and pure water. Water deionized to 16 MΩ cm resistivity was used as subphases.

Monolayers of RuL(EIN)₂, TAMRA, CeL₂, EP-PDI and TPyP were formed by spreading 480 μL, 320 μL, 720 μL, 530 μL and 300 μL of corresponding solutions on the surface of the subphase. Spreading was done by using an automatic micropipette (Gilson, France) delivering 5 μL drops onto a subphase surface in a chessboard-like pattern to distribute the monolayer uniformly. The solvent was allowed to evaporate for 15-20 min prior to the monolayer compression. For preparing the ultrathin films the monolayers were compressed until certain surface pressure was achieved (for RuL(EIN)₂ – 3, TAMRA – 20, CeL₂ – 1, EP-PDI – 18, TPyP – 20 mN·m⁻¹ respectively). The compressed films were deposited vertically with automatic dipper onto the various supports (piranha-pretreated silicon wafers, quartz glass and freshly cleaved mica).

Formation and Tuning of Plasmonic Antennas

The equimolar solution of SA and ODA in chloroform was obtained by mixing of solutions of individual components; the mixed solution was used immediately after preparation. The interfacial films were formed by spreading the SA/ODA mixture on the surface of colloidal solutions in glass vessels of known diameter at 20±1°C. The amount of spread solution should correspond to the surface coating, in which the area per molecule of surfactant is close to that in a tightly packed Langmuir monolayer (ca. 20 Å²).⁴⁹ Spreading was done using an automatic micropipette (Gilson) delivering 1μL drops onto a subphase surface in a chessboard-like pattern to distribute the monolayer uniformly.

The as-formed floating mixed SA/ODA films with adsorbed nanoparticles were deposited vertically with the transferring speed 5 mm·min⁻¹ (for percolated HTPA) or horizontally (for mixed CeO₂NP/AuNP structures) with automatic dipper onto the supports. For preparing

controls, the HTPAs with desired characteristics were deposited onto the cleaned quartz glass as well as onto the LB monolayer of stearic acid deposited onto the glass support at surface pressure $25 \text{ mN}\cdot\text{m}^{-1}$ and area per molecule 20.3 \AA^2 . The discrepancy between the integral extinctions of the controls did not exceed 5%.

UV-vis spectroscopy

UV-vis absorption/reflection spectra of organic monolayers and extinction spectra of HTPAs at the air/water interface were measured with fiber optic CCD spectrometer AvaSpec-2048 (Avantes) equipped with a 75 W DH-2000 deuterium-halogen light source (Ocean Optics). The light was incident with an angle of 90° to the film at the air-water interface and the reflected light from the surface was analyzed from 250 to 800 nm at $20\pm 1^\circ\text{C}$. The UV-vis spectra were recorded with a time resolution down to 1 min after the monolayer was spread and solvent evaporated. The spectral response measured from the monolayer-covered subphase was normalized to that obtained from the monolayer-free subphase (water, gold hydrosol or hydrosols mixture), using AvaSoft supplied by the manufacturer and further transformed into reflection and extinction spectra. The spectra of solutions and monolayers of $\text{RuL}(\text{EIN})_2$, TAMRA, CeL_2 , EP-PDI, TPYP and HTPAs and hybrid systems transferred onto quartz were measured using a two-beam spectrophotometer Shimadzu UV-2450.

Atomic Force Microscopy (AFM)

Atomic force microscopy images were obtained by the scanning probe microscope SOLVER P47-PRO (NT-MDT). Semicontact mode was used. High resolution noncontact/semicontact “Golden” silicon AFM probes NSG01 series (NT-MDT) were used. The amplitude of the “free air” probe oscillations was from 20 to 25 nm (peak-to-peak).

Scanning Electron Microscopy (SEM)

Scanning electron microscopy images of LB films were obtained using a NVision 40 workstation (Carl Zeiss) at 1 and 5 kV accelerating voltages using secondary electron (SE2) detector. To distinguish between objects of different atomic composition, a back scattered

electron (BSE) detector was also used. SE and BSE images were taken from the same spots to separate topographic and compositional contrast. The silica or quartz-supported films were scanned at an electron beam accelerating voltage of 5 kV. The selection of the HTPA controls was performed by counting nanoparticles at 30 randomly selected 100×100 nm sites. For optical studies, only the pairs of hybrid film and corresponding control for which the discrepancy in the number of particles did not exceed 10%, were used.

Confocal Laser Scanning Microscopy

Fluorescent images were obtained locally by confocal laser scanning microscope (CLSM) Olympus FluoView FV1000 equipped with spectral version scan unit based on motorized inverted microscope Olympus IX82. Excitation wavelength was 405 nm.

Computer simulation

The optical properties of hybrid systems consisting of an organic dye layer and a single gold nanoparticle were simulated by the finite difference time domain (FDTD) method. A trial version of the FDTD Solutions (Lumerical) program with a 30-day license was used for the calculations.

S1. Optical efficiency and comparative analysis of optical properties of AuNPs and organic chromophores

The optical efficiency of a material is defined as the optical extinction cross section σ_{ext} divided by the geometric cross section σ_{geom} . Reporting optical efficiency rather than optical extinction cross section rescales the optical intensity by the nanoparticle size. Because both the optical and geometric cross sections have units of length squared, the optical efficiency is a unit-less parameter.

Whereas calculating the geometric cross section of spherical particles is a straightforward procedure, the determination of the geometric cross section of rods, pyramids, and triangular or disc-like plates is more complex. There is a number of conventionally used approaches. The most common one applies a cross section of $\pi \cdot R_{\text{eff}}^2$, where $R_{\text{eff}} = (3V/4\pi)^{1/3}$. V in this expression is the total volume of the nanomaterials, i.e., molecule or nanoparticles, defining the geometric cross as a cross section of a sphere, which volume is equal to that of nonspherical material.

For an AuNP with a diameter of 20 nm, $\sigma_{\text{geom}} = \pi \cdot R_{\text{eff}}^2 \approx \pi \cdot (1 \times 10^{-6} \text{ cm})^2 = 3.1 \times 10^{-12} \text{ cm}^2$. The value of σ_{abs} for the AuNP in H_2O ($n=1.33$) is $387 \text{ nm}^2 = 3.9 \times 10^{-12} \text{ cm}^2$.¹ Thus, the optical efficiency of this AuNP in H_2O is about 1.3.²

For well-known dye rhodamine 6G, which can be considered as an example in our calculations, molar extinction ϵ_M at 530 nm is about $1.2 \times 10^5 \text{ M}^{-1} \cdot \text{cm}^{-1}$.³ Absorption cross-section σ_{abs} for Rhodamine 6G molecule calculated by equation $\sigma_{\text{abs}} = \log_{10}(1 \times 10^3/N_A) \cdot \epsilon_M = 3.8 \times 10^{-21} \cdot \epsilon_M = 4.6 \times 10^{-16} \text{ cm}^2$. Molar volume of the rhodamine 6G molecule can be calculated from the density 1.25 g/cm^3 and molar mass $4.4 \times 10^2 \text{ g/mol}$. Molar volume is $3.5 \times 10^2 \text{ cm}^3/\text{mol}$ and the volume of one molecule is $5.8 \times 10^{-22} \text{ cm}^3$. R_{eff} of rhodamine 6G molecule is $5.2 \times 10^{-8} \text{ cm}$ (i.e. about 5 Å) and σ_{geom} of rhodamine 6G molecule is $8.4 \times 10^{-15} \text{ cm}^2$. Thus, the optical efficiency of rhodamine 6G at 530 nm is 0.06.

For the substances used in this work the optical efficiency values at the wavelength corresponding to maxima of absorbance were estimated based on the solution absorbance spectra as:

RuL(EIN)₂ – 0.06 at 325 nm and 0.03 at 625 nm;

TAMRA – 0.04 at 350 nm and 0.04 at 545 nm;

CeL₂ – 0.04 at 355 nm, 0.01 at 480 nm, 0.04 at 645 nm and 0.02 at 690 nm;

EP-PDI – 0.01 at 455 nm, 0.03 at 490 nm and 0.05 at 525 nm;

TPyP – 0.06 at 420 nm, 0.01 at 515 nm and less than 0.01 at 550 nm, 590 nm and 645 nm.⁴

All these values are significantly less than that of typical optical efficiency for 20-nm AuNP which is about 1 in the order of magnitude.

S2. Properties of RuL(EIN)₂ chromophore in solution and Langmuir monolayers

1

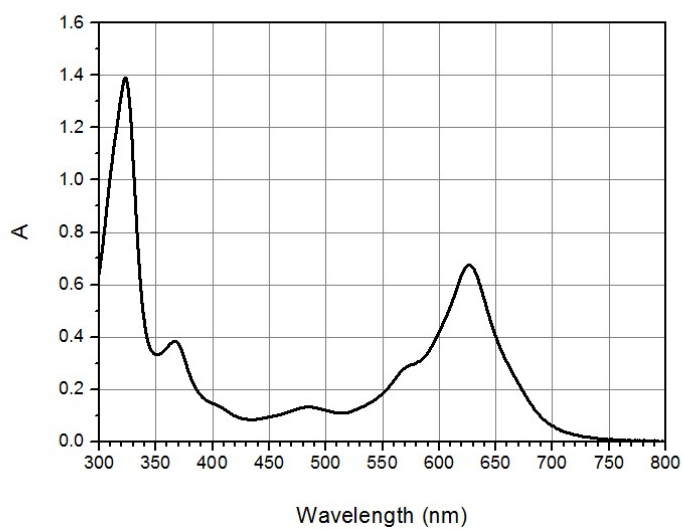


Fig. S1 UV-vis spectrum of RuL(EIN)₂ solution in chloroform ($c = 5 \cdot 10^{-5}$ M).

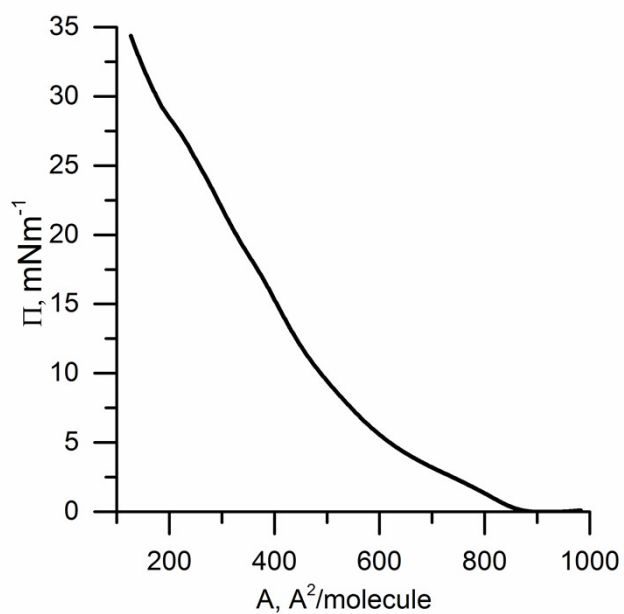


Fig. S2 Π -A isotherm of RuL(EIN)₂ monolayer spread from $5 \cdot 10^{-5}$ M chloroform solution.

I

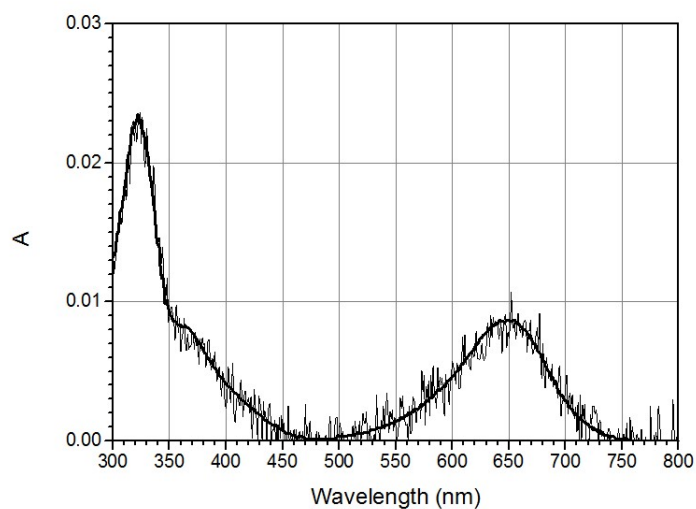


Fig. S3 UV-vis spectrum of RuL(EIN)₂ monolayer recorded at the air/water interface at surface pressure 3 mN·m⁻¹.

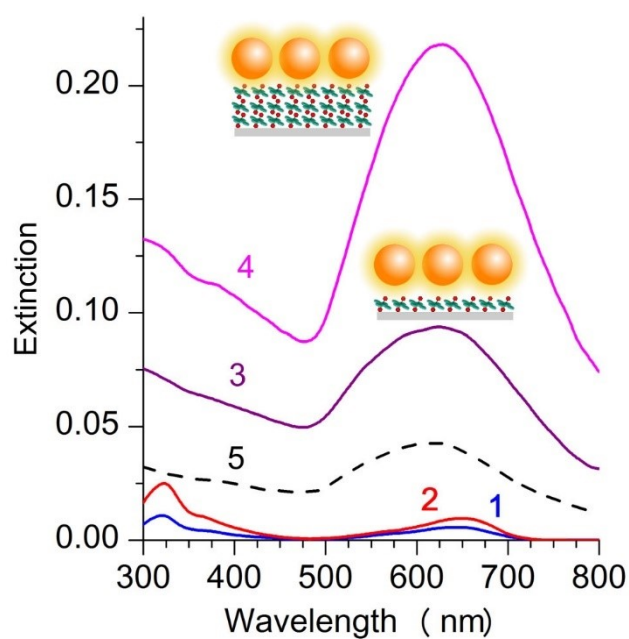


Fig. S4. UV-vis spectra of the RuL(EIN)₂ monolayer film (1), three layers of dye (2), and the same PA structure immobilized on the surface of dye monolayer (3) and 3-layer film (4), respectively. For the detailed spectra of both organic films, see Figure S5. Dashed line (5) represents the typical spectrum of control PA; the structures of hybrid films are drawn schematically.

I

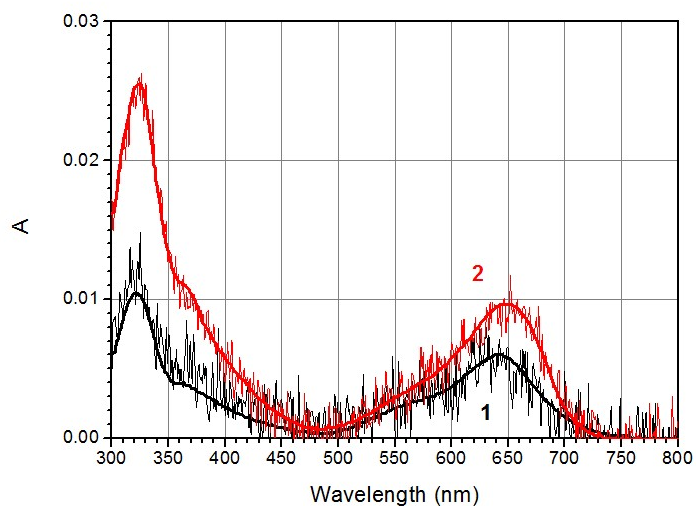


Fig. S5 UV-vis spectrum of RuL(EIN)₂ monolayer (1) and three layers of dye (2) transferred vertically onto the quartz glass.

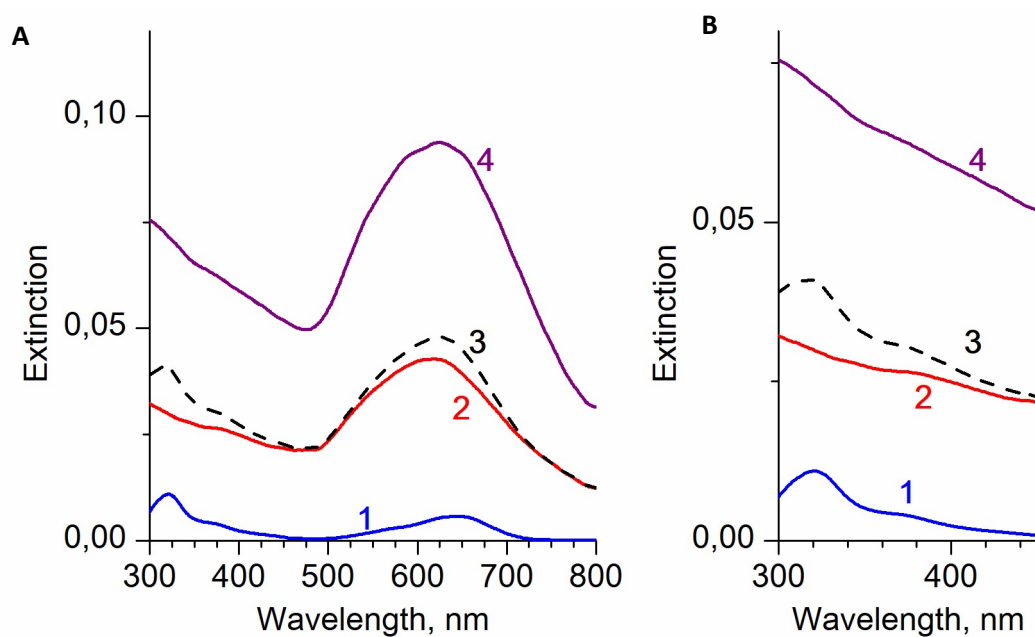


Figure S6. UV-vis spectra of RuL(EIN)₂ coating (1), control PA of AuNPs having tuned position of LSP band at 635 nm (2) and hybrid RuL(EIN)₂/PA bilayer (4); curve 3 represents a calculated spectral sum of 1 and 2: (a) the full spectrum of the hybrid and (b) the region of the Soret band of RuL(EIN)₂.

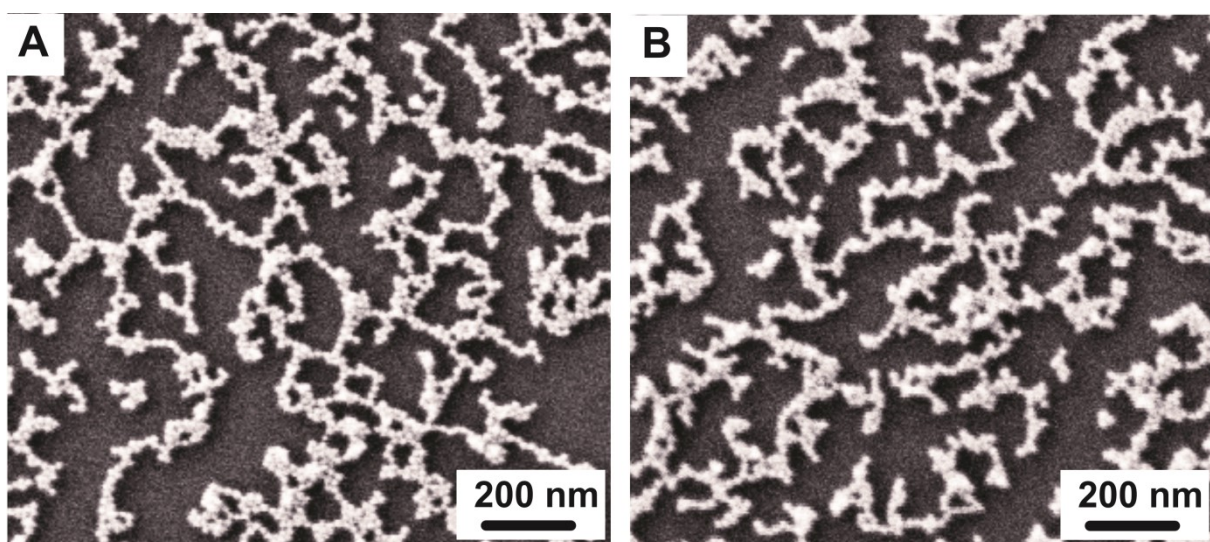


Fig. S7 SEM microphotographs of plasmonic structure on the surfaces of (a) RuL(EIN)₂ film on silicon wafer support and (b) pre-cleaned silicon wafer.

S3. Properties of TAMRA chromophore in solution and Langmuir monolayers

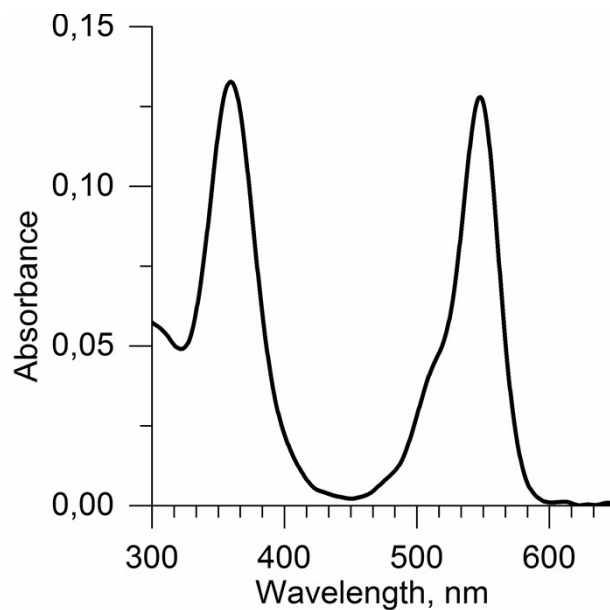


Fig. S8 UV-vis spectrum of TAMRA solution in chloroform ($c = 1 \cdot 10^{-5}$ M).

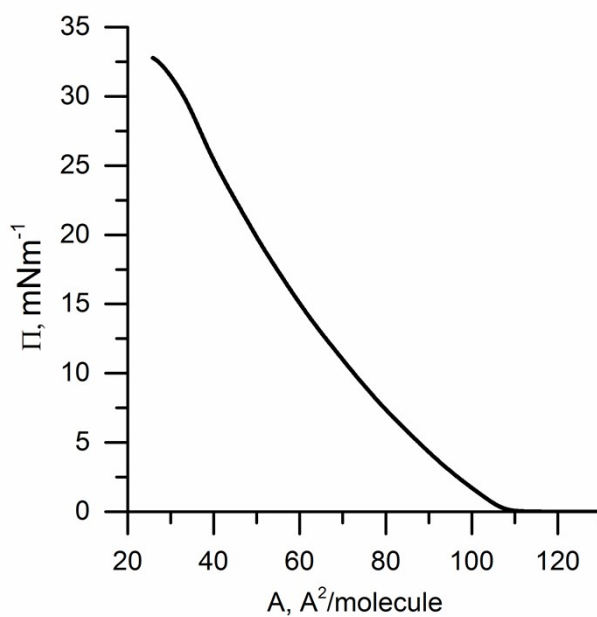


Fig. S9 Π -A isotherm of TAMRA monolayer spread from 10^{-5} M chloroform solution at the air/water interface.

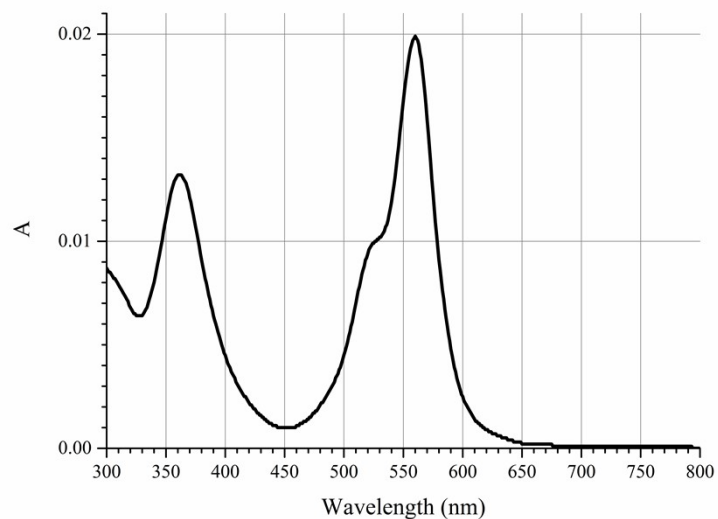


Fig. S10 UV-vis spectrum of TAMRA monolayer recorded at the air/water interface at surface pressure $20 \text{ mN}\cdot\text{m}^{-1}$.

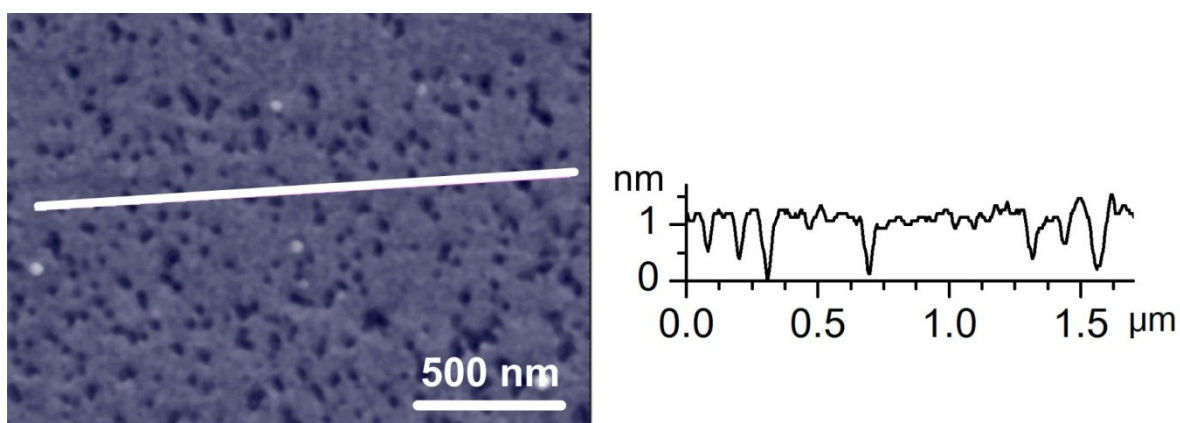


Fig. S11 AFM image and corresponding surface profile of TAMRA monolayer transferred onto mica support at surface pressure $20 \text{ mN}\cdot\text{m}^{-1}$.

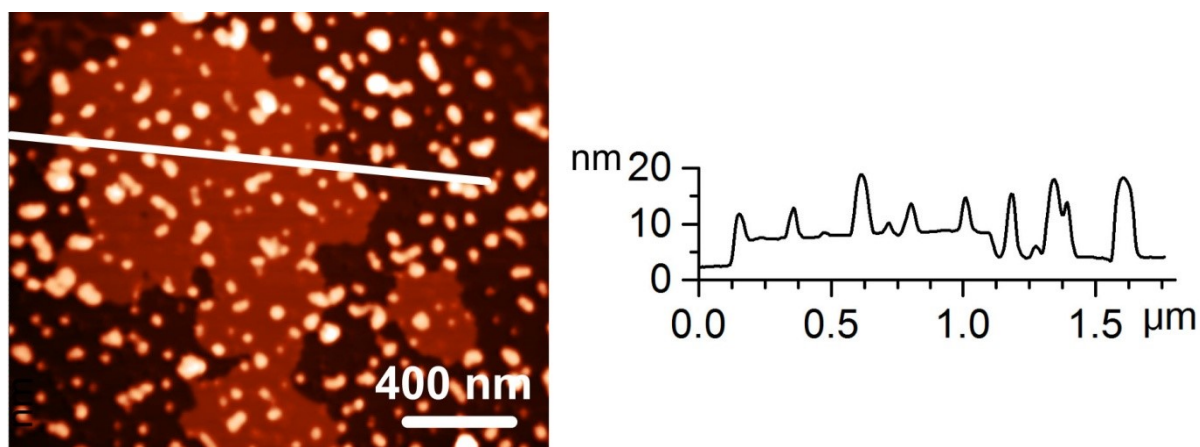


Fig. S12 AFM image and corresponding surface profile for the control CeO₂NPs/AuNPs monolayer deposited onto the mica support.

S3.1 The plasmonics antenna presenting mostly dimers and separated particles was additionally stabilized by optically transparent ceria nanoparticles with high refractive index to prevent rupturing during the transfer process. The antenna was formed by the entrapping of AuNPs within a surfactant-stabilized film of 3-nm CeO₂ nanoparticles (CeO₂NPs) on the surface of mixed colloidal solutions. By varying the ratio of AuNPs to CeO₂NPs in the solution, one can tune the position of LSP band in the resulting film. For details, see Experimental Section in the main text and Ref. ⁵.

S3.2 Control experiments showed that the immobilization of a single-component colloid presenting only CeO₂NPs in the surfactant matrix did not influence the spectrum of the TAMRA film.

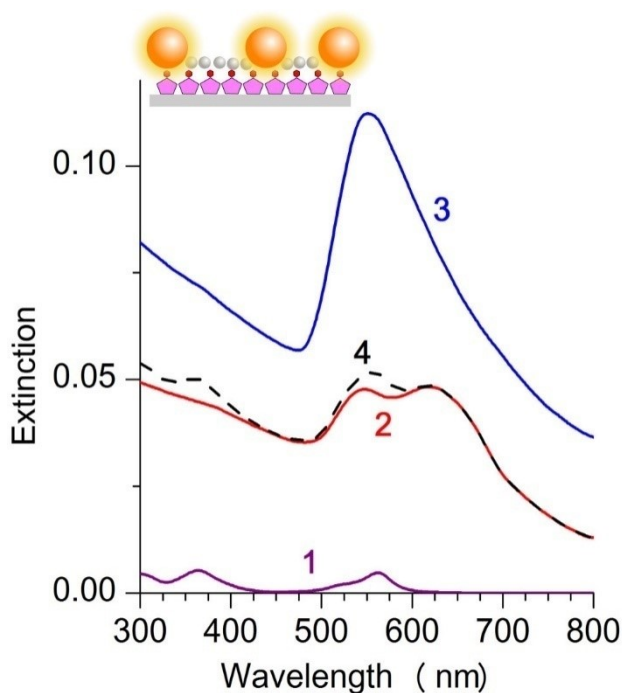


Fig. S13. UV-vis spectra of TAMRA coating (1), control binary PA of CeO₂NPs/AuNPs with a component ratio 80:1 (2), and hybrid TAMRA/PA bilayer (3); curve 4 represents a calculated spectral sum of 1 and 2. The hybrid structure is drawn schematically. For AFM image and corresponding surface profile of the CeO₂NPs/AuNPs antenna, see Figure S11.

S4. Properties of CeL₂ chromophore in solution and Langmuir monolayers

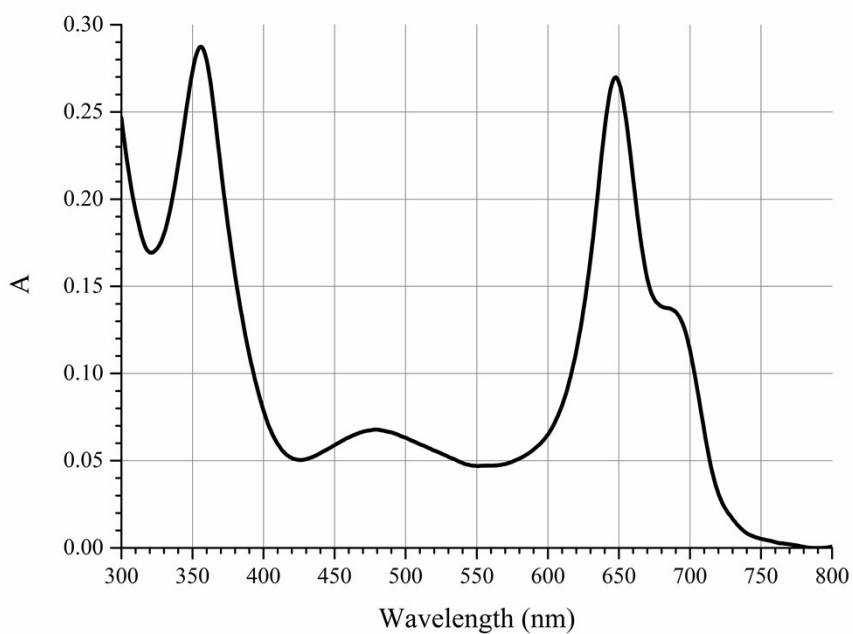


Fig. S14 UV-vis spectrum of CeL₂ solution in chloroform ($c = 1 \cdot 10^{-5}$ M).

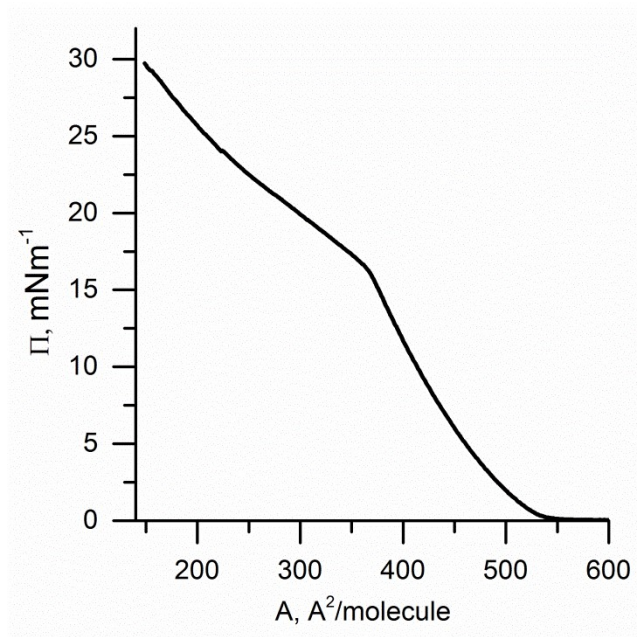


Fig. S15 Π -A isotherm of CeL₂ monolayer spread from 10^{-5} M chloroform solution at the air/water interface.

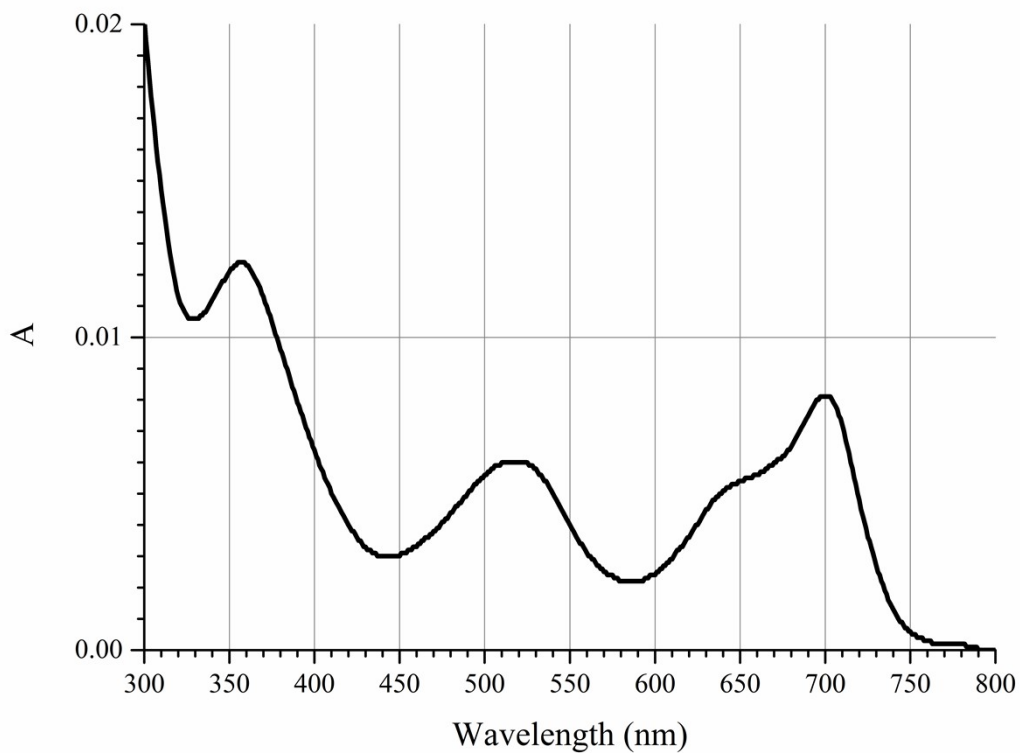


Fig. S16 UV-vis spectrum of CeL₂ monolayer recorded at the air/water interface at surface pressure 1 mNm⁻¹.

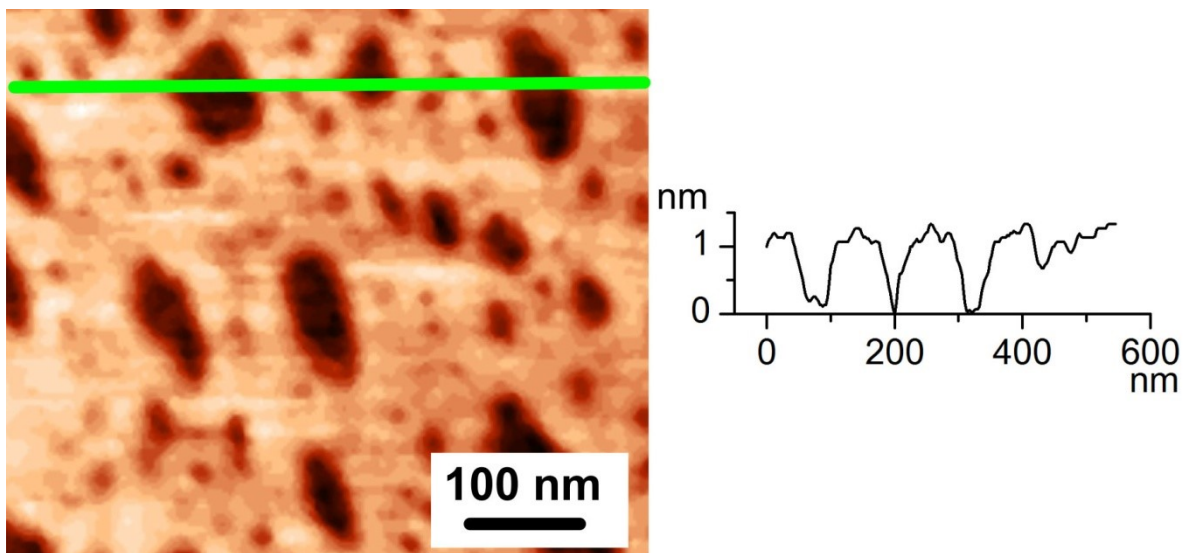


Fig. S17 AFM image and corresponding surface profile of CeL₂ monolayer transferred onto mica support at surface pressure 1 mNm⁻¹.

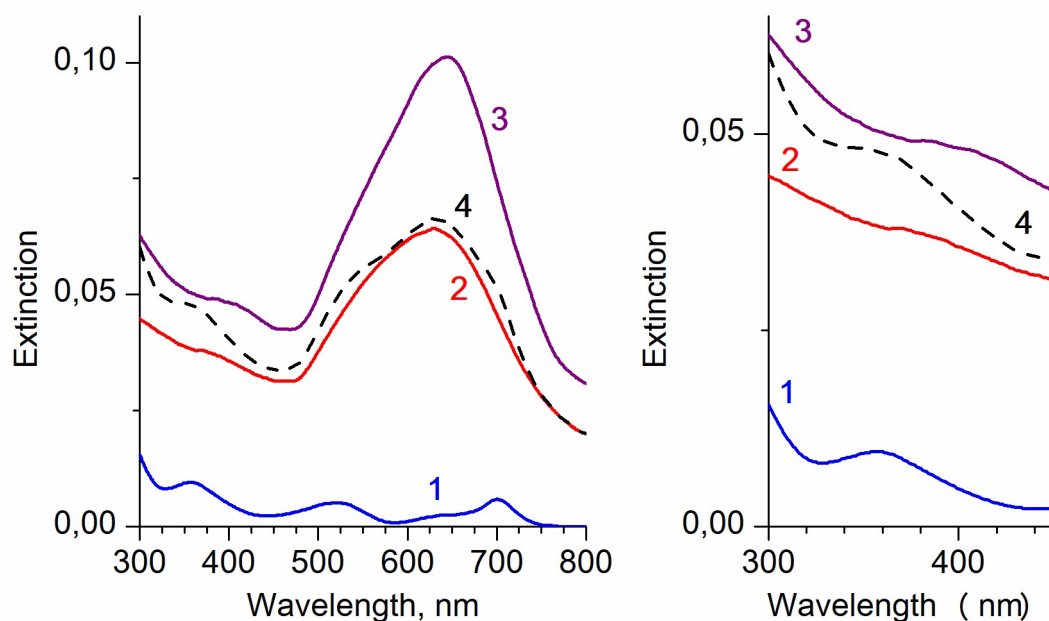


Figure S18. UV-vis spectra of CeL₂ coating (1), control PA of AuNPs having tuned position of LSP band at 635 nm (2) and hybrid CeL₂/PA bilayer (3); curve 4 represents a calculated spectral sum of 1 and 2. Shown the full spectral region (a) and the region of the Soret band of CeL₂ films: (a) the full spectrum of the hybrid and (b) the region of the Soret band of CeL₂.

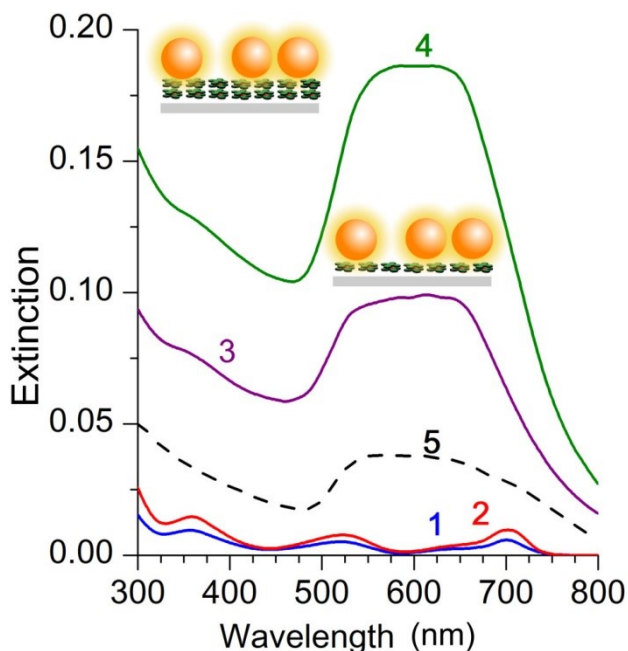


Fig. S19 UV-vis spectra of the CeL₂ monolayer film (1), incomplete bilayer of dye (2) transferred at surface pressure 1 mN·m⁻¹, and the same PA structure immobilized on the surface of dye monolayer (3) and bilayer (4), respectively. Dashed line (5) represents the typical spectrum of control PA. For the detailed spectra of both organic films, see Figure S18.

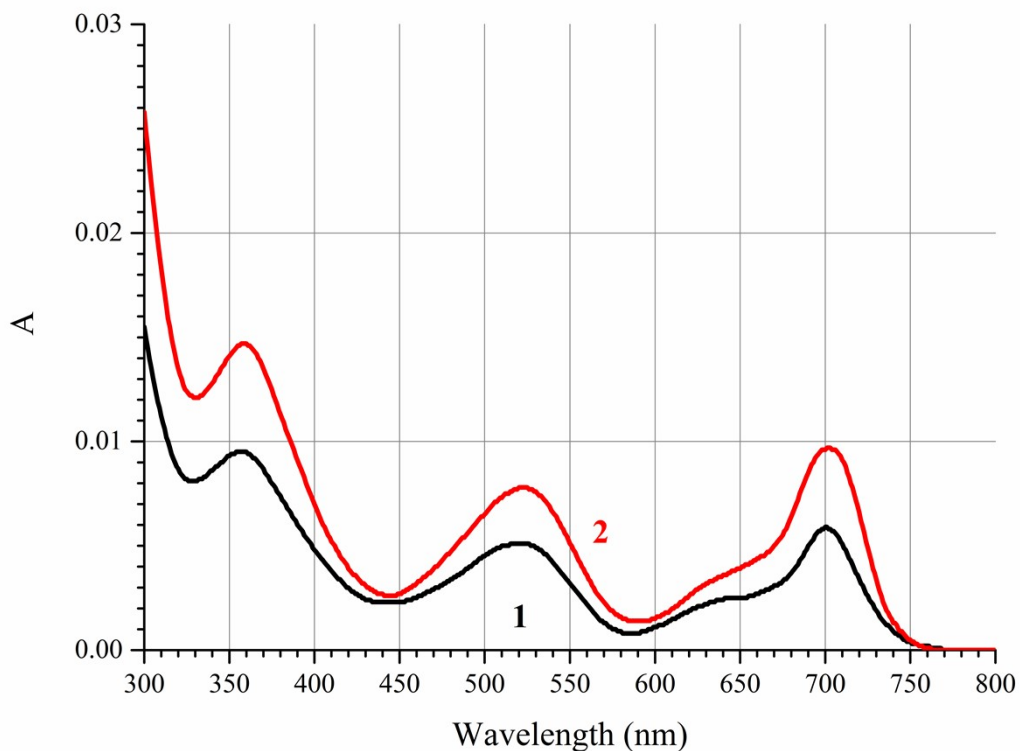


Fig. S20 UV-vis spectra of the monolayer (1) and bilayer of CeL₂ (2) transferred at quartz glass at surface pressure 1 mN·m⁻¹.

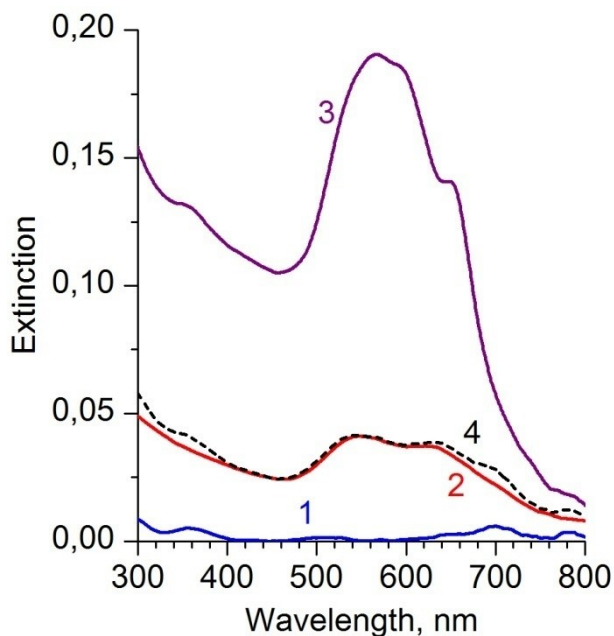


Fig. S21 UV-vis spectra of CeL₂ monolayer with edge-on orientation of molecules transferred at surface pressure 20 mNm⁻¹ (1), control PA of AuNPs with maximal absorbance at 550 and 630 nm (2), and hybrid CeL₂/PA structure (3); curve 4 represents a calculated spectral sum of 1 and 2.

S5. Properties of EP-PDI chromophore in solution and Langmuir monolayers

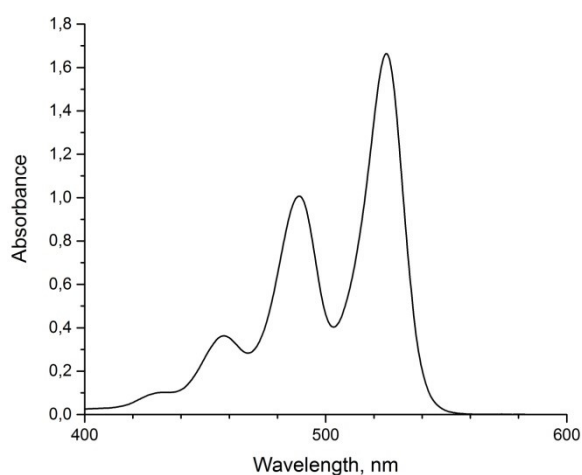


Fig. S22 UV-vis spectrum of EP-PDI solution in chloroform ($c = 1.4 \cdot 10^{-4}$ M).

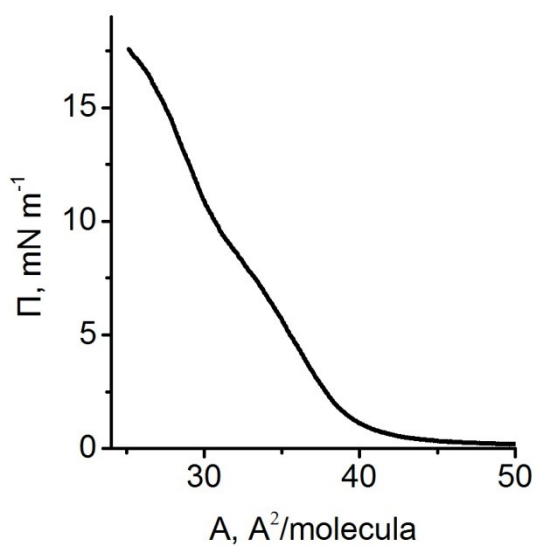


Fig. S23 Π -A isotherm of EP-PDI monolayer spread from $1.4 \cdot 10^{-4}$ M chloroform solution at the air/water interface.

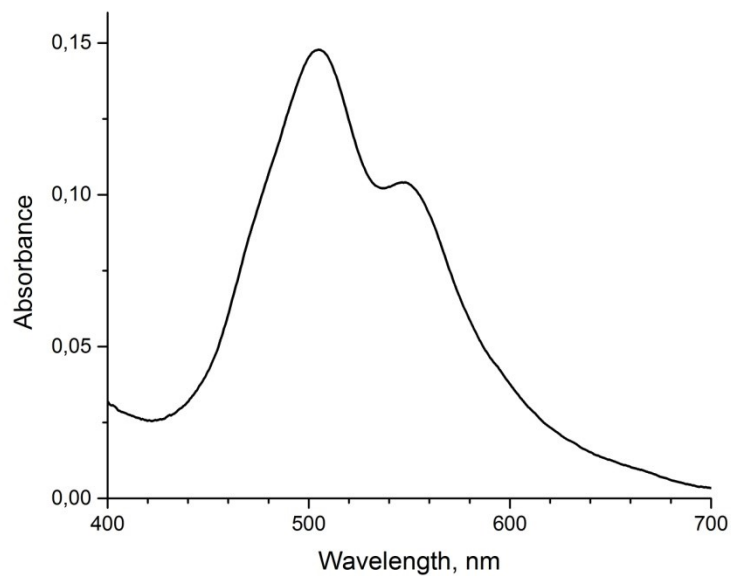


Fig. S24 UV-vis spectrum of EP-PDI monolayer recorded at the air/water interface at a surface pressure 18 mNm^{-1} .

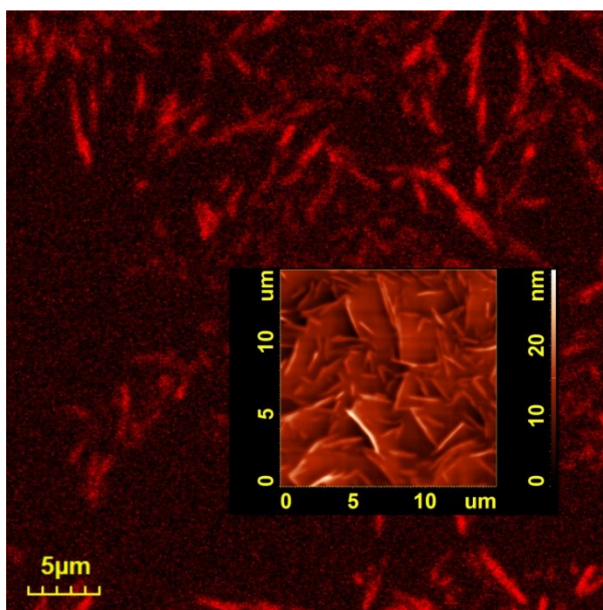


Fig. S25 CLSM fluorescent image of EP-PDI film transferred onto mica support at a surface pressure $18 \text{ mN}\cdot\text{m}^{-1}$. Excitation wavelength is 405 nm; emission bandwidth is 640-690 nm.

S6. Properties of TPyP chromophore in solution and Langmuir-Blodgett films

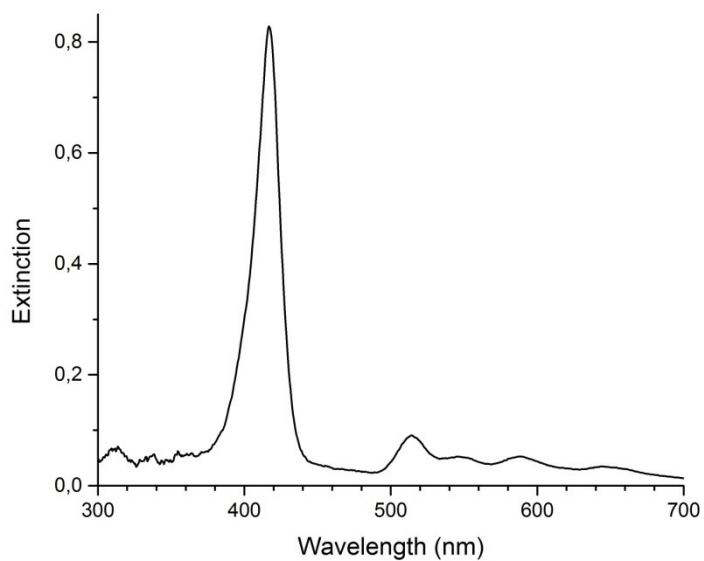


Fig. S26 UV-vis spectrum of TPyP solution in chloroform ($c = 5 \cdot 10^{-5}$ M).

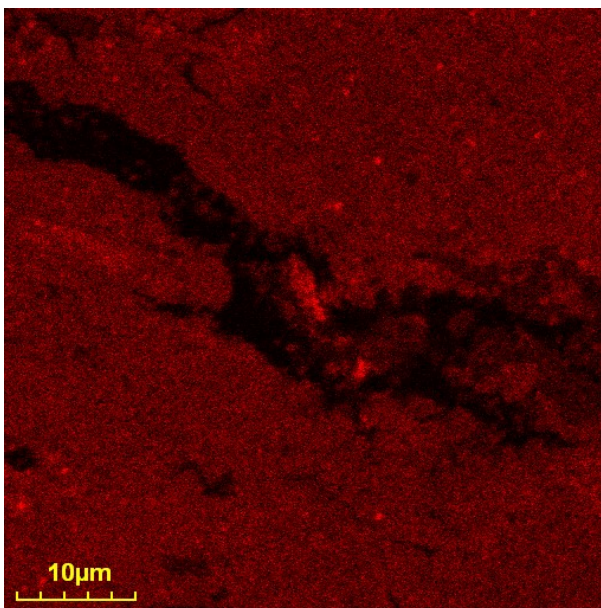


Fig. S27 CLSM fluorescent image of hybrid TPyP film transferred onto quartz glass support at a surface pressure $20 \text{ mN} \cdot \text{m}^{-1}$. Excitation wavelength is 405 nm, emission bandwidth is 640-690 nm.

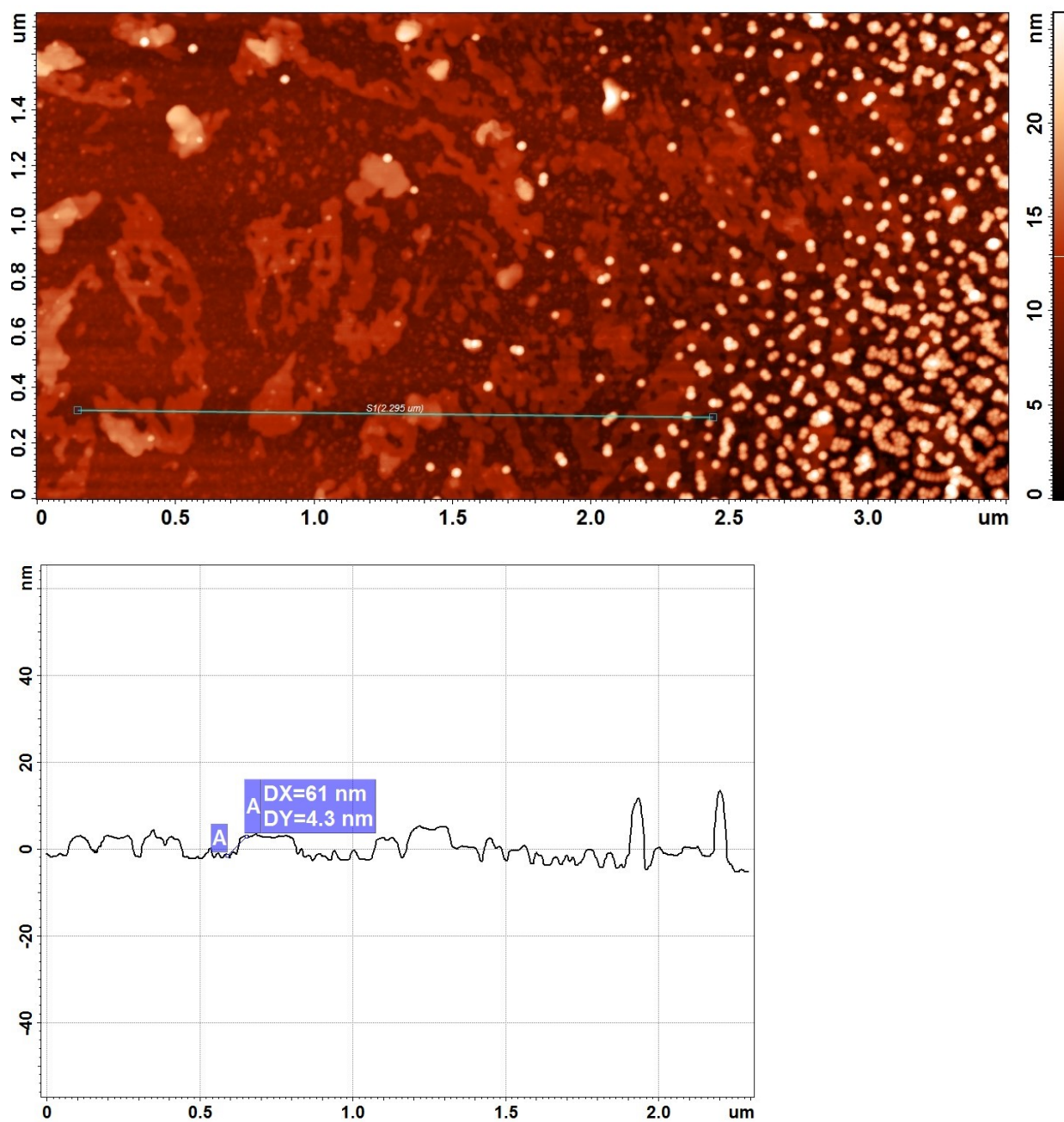


Fig. S28 AFM image and corresponding surface profile of hybrid TPyP/AuNPs structure on the surface of quartz glass.

S7. Influence of the dielectric properties of the media on the optical properties of AuNP

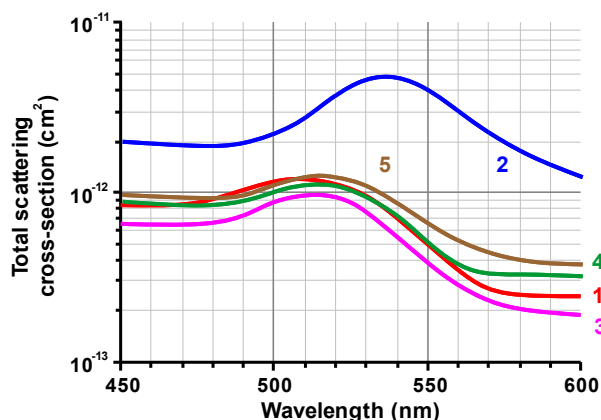
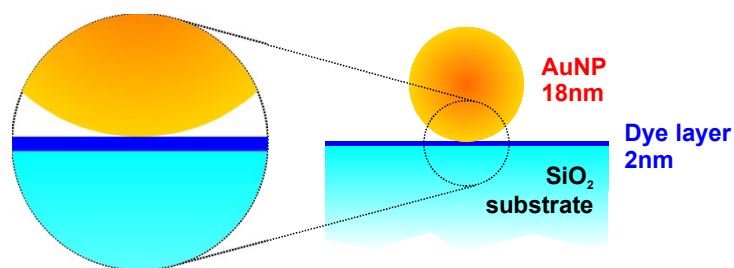
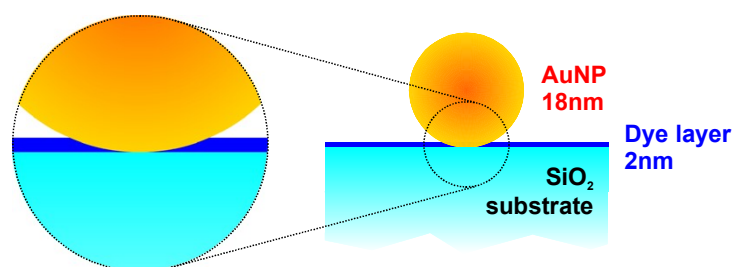


Fig. S29. Numerical calculation results of the scattering of AuNP in vacuum (1), embedded into the quartz glass (2), placed on the quartz glass surface (3), placed on the 2 nm dye layer deposited on the quartz glass surface (4) (diagram of the sample is presented in Fig. S28a) and embedded into the 2 nm dye layer deposited on the quartz glass surface (5) (diagram of the sample is presented in Fig. S28b). Total scattering cross-section is a sum of absorption and scattering cross-sections.



a



b

Fig. S30. Schematic diagrams of AuNP placed on the 2 nm dye layer deposited on the quartz glass surface (a) and embedded into the 2 nm dye layer deposited on the quartz glass surface (b).

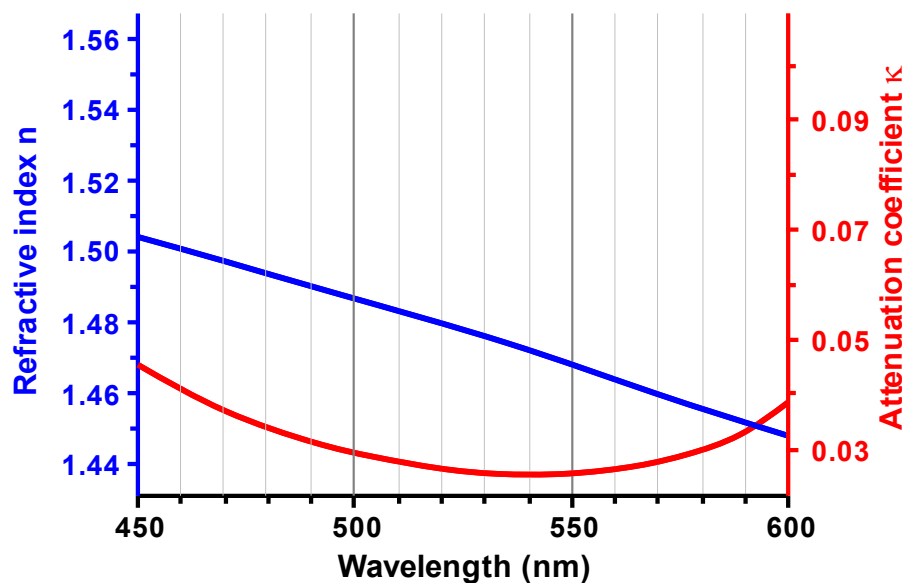


Fig. S31. Complex refractive index of model dye used during the FDTD calculations.

S8. Numerical simulation of the near field of the AuNPs on the dye-coated solid surface

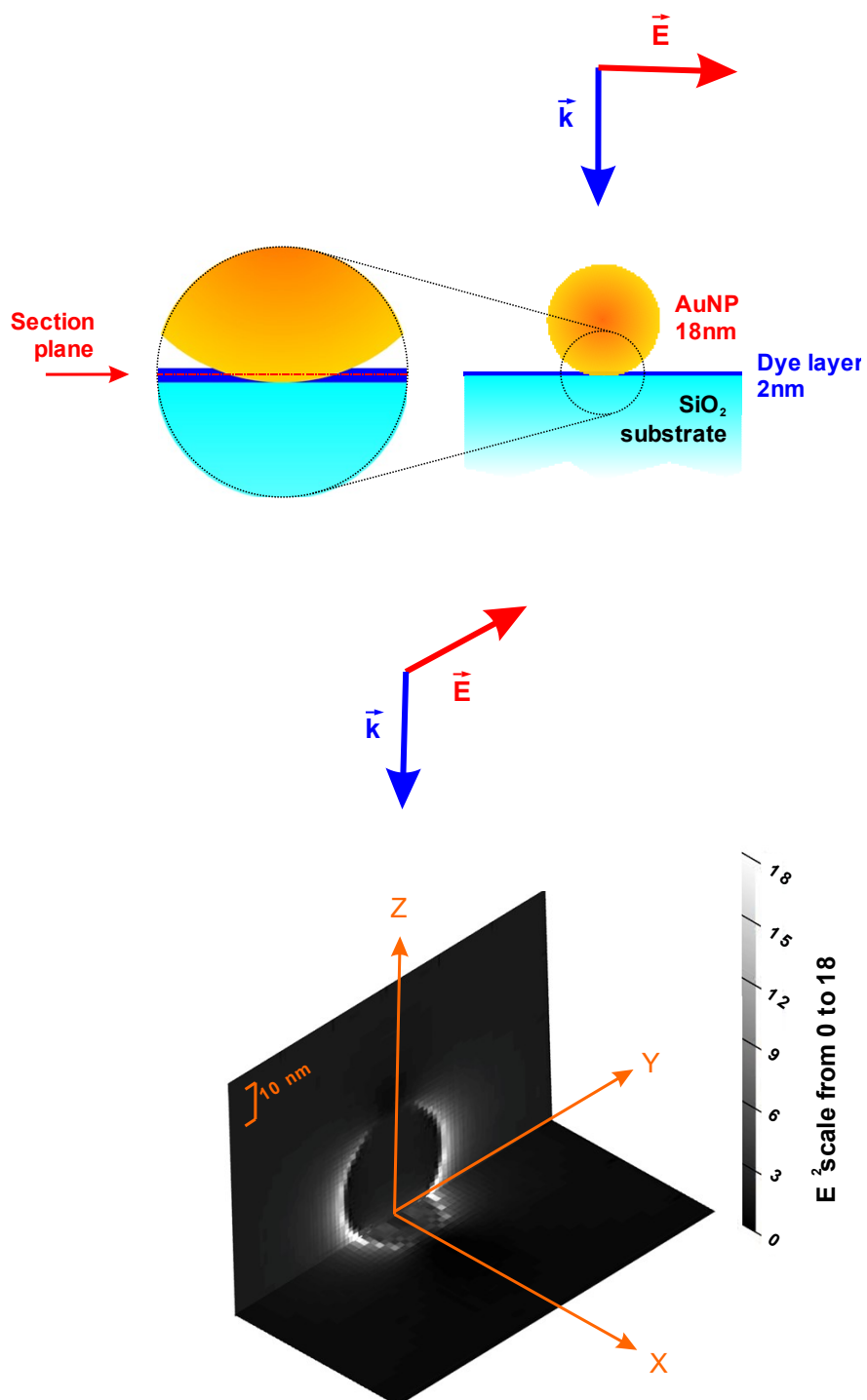


Fig. S32. Scheme of the calculated system and the near field distribution around of AuNP intercalated into the 2 nm dye layer deposited on the quartz glass surface. Wavelength of the incident light is 520 nm

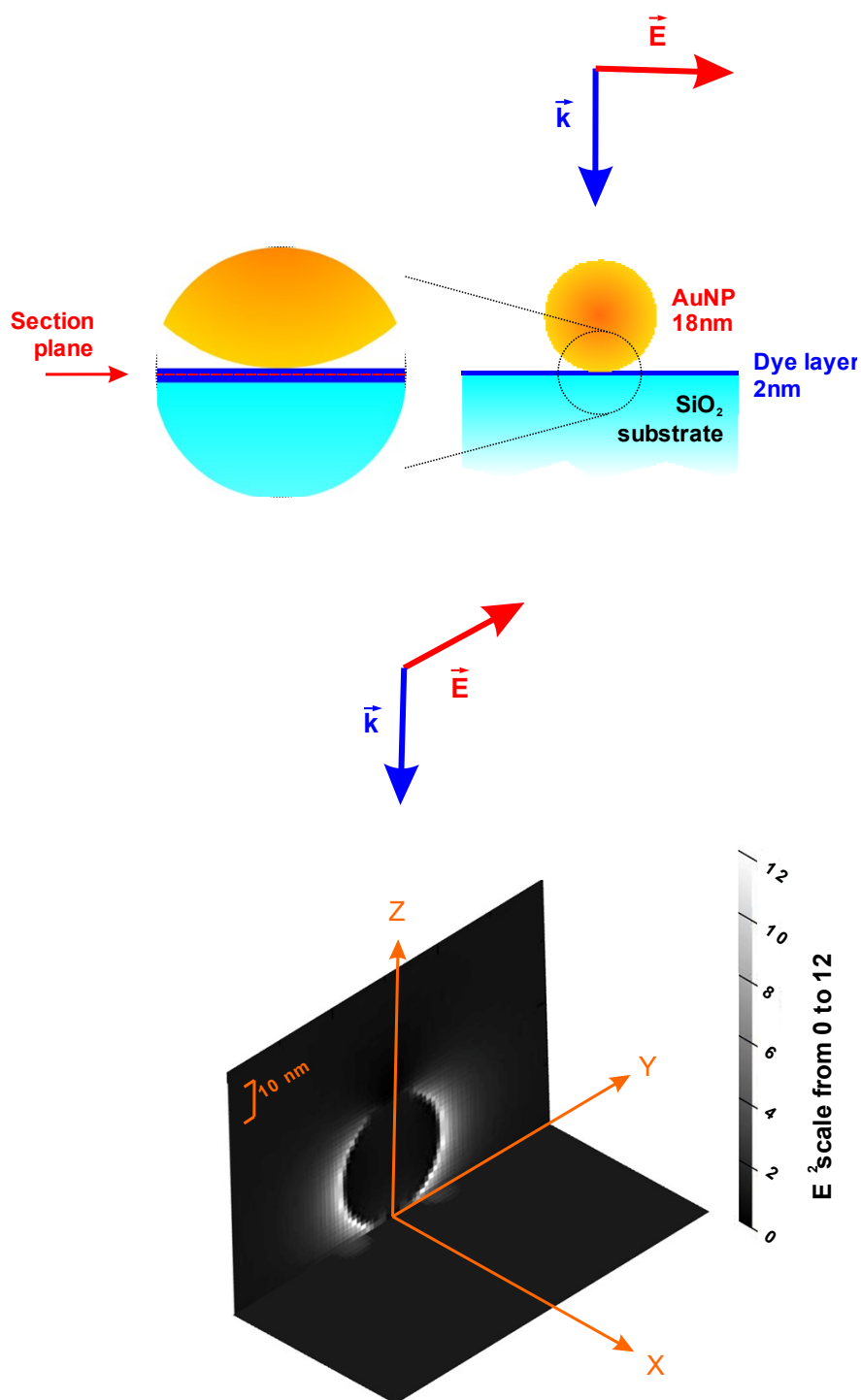


Fig. S33. Scheme of the calculated system and near field distribution around of AuNP placed on top of the 2 nm dye layer deposited onto the quartz glass surface. Wavelength of the incident light is 520 nm.

For FDTD simulations, we considered the configuration, in which the particles and the dyes are on the surface of the substrate, and the incident light falls normal to this substrate. The results of simulations show that, for the AuNP partially embedded into the thin layer of dye, the localized and enhanced optical near field of this AuNP is concentrated around the particle both in the air and in the dye layer (Fig.S30). This is the cause of an increase of absorption of near field by the dye in the close proximity of AuNP. In the far field framework, it can be described as an enhancement of absorption of the dye caused by AuNPs. This is the case of non-additive

increase of absorption, when no optical effects associated with the collective optical behavior of molecules occur.

When the AuNP is deposited on the surface of the dye layer, AuNP does not localize and does not enhance near field in this layer. Although it is actually enhanced and localized, the near field propagates outside of the dye layer. This is the case of additive optical properties of AuNPs and dye (Fig.S31).

When the dye forms J-aggregates, they exhibit characteristic absorption spectra because of optically collective behavior of molecules in these aggregates due to the strong intermolecular interactions. The penetration of AuNPs into such structure would result in its decomposition and in the change of its optical properties. Even though such decomposition affects a small portion of the J-aggregate, we have to take into account that the enhancement of near field is also spatially localized. That is, the interactions between AuNP and the aggregate should either change the optical properties of the aggregated dye or they should not lead to the enhanced absorption.

S9. References

- 1 A. Gaiduk, P. V. Ruijgrok, M. Yorulmaz and M. Orrit, *Chem. Sci.*, 2010, **1**, 343–350.
- 2 M. Loumagne, C. Midelet, T. Doussineau, P. Dugourd, R. Antoine, M. Stamboul, A. Débarre and M. H. V. Werts, *Nanoscale*, 2016, **8**, 6555–6570.
- 3 K. Tóth and J. Langowski, .
- 4 L. Monsù Scolaro, M. R. Plutino, A. Romeo, R. Romeo, G. Ricciardi, S. Belviso and A. Albinati, *Dalt. Trans.*, 2006, 2551–2559.
- 5 A. I. Zvyagina, A. A. Ezhov, V. K. Ivanov, V. V. Arslanov and M. A. Kalinina, *J. Mater. Chem. C*, 2015, **3**, 11801–11805.